*American Mineralogist, Volume 107, pages 885–895, 2022*

# Synthesis, structure, and single-crystal elasticity of Al-bearing superhydrous phase B

**Xinyang Li[1,2,*], Sergio Speziale[2], Konstantin Glazyrin[1], Franziska D.H. Wilke[2], Hanns-Peter Liermann[1], and Monika Koch-Müller[2]**

[1]Deutsches Elektronen-Synchrotron (DESY), 22607 Hamburg, Germany
[2]GFZ German Research Centre for Geosciences, Telegrafenberg, 14473 Potsdam, Germany

## Abstract

Dense hydrous magnesium silicates (DHMSs) with large water contents and wide stability fields are a potential $H_2O$ reservoir in the deep Earth. Al-bearing superhydrous phase B (shy-B) with a wider stability field than the Al-free counterpart can play an important role in understanding $H_2O$ transport in the Earth's transition zone and topmost lower mantle. In this study, a nominally Al-free and two different Al-bearing shy-B samples with 0.47(2) and 1.35(4) Al atoms per formula unit (pfu), were synthesized using a rotating multi-anvil press. Their single-crystal structures were investigated by X-ray diffraction (XRD) complemented by Raman spectroscopy and Fourier-transform infrared spectroscopy (FTIR). Single-crystal XRD shows that the cell parameters decrease with increasing Al-content. By combining X-ray diffraction and spectroscopy results, we conclude that the Al-poor shy-B crystallizes in the *Pnn*2 space group with hydrogen in two different general positions. Based on the results of the single-crystal X-ray diffraction refinements combined with FTIR spectroscopy, three substitutions mechanisms are proposed: $2Al^{3+} = Mg^{2+} + Si^{4+}$; $Mg^{2+} = \square^{Mg^{2+}} + 2H^+$ ($\square^{Mg^{2+}}$ means vacancy in Mg site); $Si^{4+} = Al^{3+} + H^+$. Thus, in addition to the two general H positions, hydrogen is incorporated into the hydrous mineral via point defects. The elastic stiffness coefficients were measured for the Al-shy-B with 1.35 pfu Al by Brillouin scattering (BS). Al-bearing shy-B shows lower $C_{11}$, higher $C_{22}$, and similar $C_{33}$ when compared to Al-free shy-B. The elastic anisotropy of Al-bearing shy-B is also higher than that of the Al-free composition. Such different elastic properties are due to the effect of lattice contraction as a whole and the specific chemical substitution mechanism that affect bonds strength. Al-bearing shy-B with lower velocity, higher anisotropy, and wider thermodynamic stability can help understand the low-velocity zone and the high-anisotropy region in the subducted slab located in Tonga.

**Keywords:** Al-bearing superhydrous phase B, crystal structure, elasticity, Brillouin scattering, X-ray diffraction

## Introduction

Several studies show the presence of hydrous minerals, such as hydrous ringwoodite, brucite, and ice-VII, as inclusions in diamonds from the deep earth interior (Pearson et al. 2014; Palot et al. 2016; Tschauner et al. 2018). This proves that the Earth's mantle is, at least locally, hydrated. $H_2O$ can be introduced into the deep Earth by subducted slabs via hydrous minerals (Schmidt and Ulmer 2004; Ohtani 2005) or originally stored in the deep Earth from the protosolar nebula material (Hallis et al. 2015; Peslier 2020). $H_2O$ could be incorporated in some nominally anhydrous minerals such as olivine, wadsleyite, and ringwoodite. However, the $H_2O$-storage capacity of these minerals is limited and lower than ~3 wt% (e.g., Mao and Li 2016). Dense hydrous magnesium silicates (DHMSs), such as Phase A, Phase E, superhydrous phase B (shy-B), phase D, and phase H with large $H_2O$ contents and wide-phase stability are thus potential $H_2O$ carriers in cold or warm subducted slabs (Ohtani 2005; Nishi et al. 2014).

Mg-end-member shy-B ($Mg_{10}Si_3H_4O_{18}$) with 5.8 wt% water has been proposed to form in the hydrated pyrolite system at the Earth's transition zone and topmost lower mantle at pressure and temperature (*P*-*T*) conditions of subducted slabs (Pacalo and Parise 1992; Frost 1999). The Mg-end-member of shy-B coexists with ringwoodite at the transition zone in the hydrous peridotite layer in subducted slab (e.g., Schmidt and Ulmer 2004; Ohtani 2005). At the depth of topmost lower mantle, shy-B will coexist with bridgmanite, phase D, $CaSiO_3$-perovskite to 30 GPa and then decompose to MgO and bridgmanite (e.g., Schmidt and Ulmer 2004; Ohtani 2005). $Al_2O_3$, as an important component in the peridotite and basalt layer of subducted slab, could be incorporated into the structure of DHMSs and bridgmanite (Pamato et al. 2015; Liu et al. 2016, 2017; Kakizawa et al. 2018). Phase D and shy-B could incorporate 50 and 31.9 wt% $Al_2O_3$ in their structures (Boffa Ballaran et al. 2010; Pamato et al. 2015; Kakizawa et al. 2018). The solubility of $Al_2O_3$ in bridgmanite reaches 21.8 mol% at 27 GPa and 2500 K (Liu et al. 2017). The partition coefficient of Al between shy-B and bridgmanite is considered to be 1.5–2.8 and increases with pressures and temperatures (Litasov and Ohtani 2003; Kakizawa et al. 2018). However, the partitioning of Al among coexisting shy-B, phase D, and bridgmanite is still experimentally unconstrained.

* E-mail: xinyang.li@desy.de


0003-004X/22/0005–885$05.00/DOI: https://doi.org/10.2138/am-2022-7989

The Mg-Si end-member of shy-B can be synthesized at high *P-T* in the range of 16–22 GPa and 1000–1550 °C (e.g., Pacalo and Parise 1992; Hazen et al. 1997; Koch-Müller et al. 2005). The structure of shy-B was first determined to be orthorhombic (space group *Pnnm*) by Pacalo and Parise (1992). The crystal structure consists of Si-O tetrahedra and octahedra with 2:1 ratio as well as Mg-O octahedra (Pacalo and Parise 1992). Koch-Müller et al. (2005) proposed that shy-B displays two different polymorphic modifications, a high-temperature form with space group *Pnnm* and a low-temperature form with space group *Pnn*2. Kakizawa et al. (2021) confirmed these findings. Different experimental techniques, including FTIR spectroscopy, nuclear magnetic resonance (NMR), single-crystal X-ray diffraction (XRD), and neutron diffraction, all reveal the presence of two distinct hydrogen positions in the structure of shy-B, which makes the structure to be compatible with *Pnn*2 space group (Koch-Müller et al. 2005, 2014; Xue et al. 2008; Trots et al. 2013).

The incorporation of F, $Ti^{4+}$, $Fe^{2+}$, and $Al^{3+}$ in the structure of shy-B affects the physical properties of this phase. The incorporation of F- could increase the incompressibility, density, and bulk velocity of shy-B (Li et al. 2020). Matrosova et al. (2019) have shown that Ti-bearing shy-B with a *Pnnm* space group has a wider stability field than the Mg-Si end-member. Fe-bearing shy-B has a much higher bulk modulus than the Fe-free end-member (Shieh et al. 2000; Li et al. 2016). The thermodynamic stability of Al-bearing shy-B expands to higher temperature with increasing Al content, such that shy-B with 31.9 wt% $Al_2O_3$ is stable up to 24 GPa and 2000 °C (Kakizawa et al. 2018). Based on the Al content and different substitution mechanisms in shy-B, two different types of shy-B were proposed by Kakizawa et al. (2018). In a recent study, Kakizawa et al. (2021) investigated an Al-bearing shy B sample with 1.9 Al pfu by FTIR spectroscopy, difference Fourier maps, and bond-distance considerations. The sample contained more than the ideal hydrogen amount and they propose, as an additional H incorporation mechanism, the complex substitution $2Mg^{2+} + Si^{4+} = 2\,Al^{3+} + 2\,H^{+} + \square^{Mg^{2+}}$ ($\square^{Mg^{2+}}$ means vacancy in Mg site). This needs further proof.

Knowing the elastic properties of shy-B is also very important for interpreting seismic anomalies in the deep transition zone and the shallow lower mantle, such as the low-velocity zone, the 720 km discontinuity and high-anisotropy zones (Rosa et al. 2015; Li et al. 2016; Yang et al. 2017). Thus, some experimental and ab initio computational studies investigated the elasticity on the Mg-end-member of shy-B with different water contents at high *P-T*, and the results were used to explain seismic anomalies in the topmost lower mantle (Pacalo and Weidner 1996; Mookherjee and Tsuchiya 2015; Rosa et al. 2015; Li et al. 2016; Yang et al. 2017). However, Al-bearing shy-B showing a much wider *P-T* stability should be considered as an even more important candidate for $H_2O$ transport and storage in the transition zone and topmost part of the lower mantle. One way to assess the hypothesis of Al-bearing shy-B phase being present in deeply subducted slabs is comparing mineralogical models with geophysical observations such as those from seismology. Here we provide information on the elasticity of shy-B as a function of the Al content.

In this study, we used a rotating multi-anvil apparatus to synthesize a nominally Al-free shy-B with 0.04(1) Al atoms per formula unit (pfu) (based on 18 O atoms pfu) and two Al-bearing shy-B with 0.47(2) and 1.35(4) Al atoms pfu. The syntheses products were analyzed with an electron microprobe (EMP), FTIR, and Raman spectroscopy. The crystal structures of the three compositions were determined by single-crystal X-ray diffraction (XRD). Finally, the elasticity of Al-rich shy-B (with 1.35 Al atoms pfu) was investigated by Brillouin scattering (BS) at ambient conditions.

## Experimental methods

### Sample syntheses using a multi-anvil apparatus

Shy-B with three different compositions were synthesized in a rotating multi-anvil press at the GFZ, Potsdam (Deon et al. 2011). This device, featuring a Walker-type high-pressure module (Walker et al. 1990), is designed to allow continuous 360° rotation of the entire press at a maximum speed of 5° per second for the duration of the synthesis. Continuous rotation enhances a homogeneous distribution of fluid and solid within the sample capsule (see Schmidt and Ulmer 2004; Deon et al. 2011). We used a 10/5 assembly (lengths of the octahedral edges and the truncations of the WC cubes, respectively) with a MgO-based octahedron serving as the pressure transmitting medium, a stepped graphite heater to avoid or minimize temperature gradients, and pyrophyllite gaskets. We monitored the sample temperature by using type C thermocouples (W5%Re-W26%Re). Details of the experimental setup are given in Mrosko et al. (2015). The starting materials were loaded in Pt capsules (length 2.25 mm, outer diameter 1.4 mm), which were cold sealed. Experimental conditions, run number, and the starting materials are summarized in Table 1.

### Electron microprobe analysis (EMPA)

Several single crystals of the synthesized shy-B were handpicked, embedded in epoxy, polished, and carbon coated to perform EMPA. The analyses were performed using a JEOL Superprobe JXA-8230 (GFZ, Potsdam) in wavelength-dispersive X-ray diffraction (WDS) mode with the following crystal-analyzers: TAP for Si and Al, LIFL for Fe, and TAPH for Mg. Although the samples do not contain Fe, Fe was required in the calibration and quality control process as the high-pressure ringwoodite standard contained iron. The microprobe was operated at 15 kV, 10 nA. The size of the measuring spot was 5 µm to prevent mineral destruction. Counting times on the peaks for Si, Al, and Mg were 10 and 20 s for Fe. Background counting times were 5 s for Si, Al, and Mg and 10 s for Fe. The standard for Mg and Si was well-characterized synthetic ringwoodite (MA-313; Mrosko et al. 2015), corundum for Al, and hematite for Fe.

### FTIR spectroscopy

FTIR spectra were measured using a VERTEX 80v FTIR spectrometer (Bruker optics) with an attached Hyperion II microscope at the IR-spectroscopy laboratory of the GFZ in Potsdam. A tungsten light source, InSb detector, and a $CaF_2$ beamsplitter were used to measure the OH stretching range (2500–4000 $cm^{-1}$). Due to the high-water content (the stoichiometric Mg-end-member has 5.8 wt% $H_2O$) a very thin film of the sample material was required and was prepared from very small amounts of the fine-grained portion of the syntheses product by pressing the material in a diamond-anvil cell (DAC) equipped with type II diamonds and without a gasket (thin-film preparation). The spectra were collected with the thin films attached to one of the diamond anvils and with 2 $cm^{-1}$ resolution and averaged over 256 scans. The reference spectra were taken through the diamonds. The thickness of the first sample (MA-575) flattened in a DAC was determined by reflecting a broadband optical probe in the collected signal scaled by the refractive index of the sample. The refractive index was estimated to be n = 1.686, which is the average value along the three crystallographic axes (Pacalo and Weidner 1996). The thickness of MA-575 is 1.0(1) µm. By optical observation, we estimated the thickness of the thin films of MA-399 and MA-576 to be 1.0 and 1.3 µm, respectively. In the absence of

**Table 1.** Composition of starting material

| Run no. | MgO (wt%) | $Mg(OH)_2$ (wt%) | $Al(OH)_3$ (wt%) | $SiO_2$ (wt%) | $H_2O$ (mL) | *P* (GPa) | *T* (°C) |
|---|---|---|---|---|---|---|---|
| MA-399[a] | 67.25 | – | – | 32.25 | 1 | 19 | 1200 |
| MA-575 | 43.8 | 21.6 | 9.9 | 24.7 | – | 19 | 1200 |
| MA-576 | 53.0 | 5.6 | 18.6 | 22.8 | – | 19 | 1200 |

[a] Using 1 mL liquid water as the water source.

a mineral-specific absorption coefficient, ε, we used the wavenumber-dependent method proposed by Libowitzky and Rossman (1997) to calculate molar absorption coefficients ε's for the bands of each sample. The spectra were deconvoluted with the software PeakFit by Jandel Scientific. We applied a Gaussian plus Lorentzian peak shape to all component bands. The integral absorbance ($A_{int}$) of each peak was summed up and multiplied by 3 to get the total integral absorbance $A_{int,tot}$. Density was derived from our single-crystal X-ray refinements, which are 3.227(3), 3.179(3), and 3.166(4) g/cm$^3$ for MA-399, MA-575, and MA-576, respectively. We used the Beer-Lambert law to calculate the water content, which can be found in Libowitzky and Rossman (1997).

Temperature-dependent thin-film spectra of samples MA-575 and MA-576 were also measured in the OH stretching region using the spectrometer and components described above in a Linkam FTIR600 cooling/heating stage adjusted to the microscope. Spectra were collected with a spectral resolution of 2 cm$^{-1}$ and averaged over 1024 scans. Shy-B thin films were investigated from ambient conditions down to –180 °C. To reach the low temperature, the stage was cooled with liquid nitrogen. The low-*T* spectra of sample MA-575 exhibited an additional peak at around 3180 cm$^{-1}$ at –180 °C, which we attributed to the formation of ice crystals visible to our eyes. In experiment MA-576 we avoided the formation of ice by annealing the sample in the Linkam sample chamber for 1 h at 100 °C while purging with nitrogen gas before the cooling experiment started.

To verify the presence of weak bands hidden in the background of the thin-film spectra, the spectra of large crystals (about 100 × 50 μm$^2$) with thicknesses varying between 30 to 60 μm were also measured in the OH stretching region using the spectrometer and components described above. The crystals were placed on KBr sample holders, and spectra were averaged over 128 scans.

FTIR spectra in the lattice vibrational range (400–2000 cm$^{-1}$) were measured using the spectrometer described above but with a Globar light source, MCT detector, and a KBr beamsplitter. The samples were prepared as thin films (see above) and placed on KBr sample holders. The spectra were collected with 4 cm$^{-1}$ resolution and averaged over 1024 scans.

## Raman spectroscopy

Raman spectra were measured with a HORIBA Jobin Yvon LabRAM HR800 VIS spectrometer (GFZ, Potsdam) equipped with a green 514 nm wavelength diode-pumped solid-state laser. The spectra were collected from the microprobe mounts after the removal of the carbon coating.

Spectra in the range of 100–1000 cm$^{-1}$ were measured for phase identification, and the data acquisition time was 30 s for MA-399 and MA-575 and 50 s for MA-576. We measured several different single crystals for MA-576—all gave much weaker signals than the crystals of the other two samples. The spectra were deconvoluted with the software PeakFit by Jandel Scientific.

Spectra in the OH stretching region were measured in the range of 3200–3600 cm$^{-1}$ with the same configuration. These measurements were extremely difficult as the samples were very sensitive to the laser light decomposition and showed high fluorescence. The Al-bearing samples were measured with 50% laser power. Spectra of MA-575 were collected for 10 s with three accumulations, while spectra of MA-576 were measured for 20 s with three accumulations.

## Single-crystal X-ray diffraction

Single-crystal XRD data were collected at the Extreme Conditions Beamline (ECB, P02.2) at PETRA III, DESY (Hamburg, Germany). To improve data quality and for the purpose of absorption correction, we pre-selected samples of a shape similar to a sphere. Samples were glued on the top of a tungsten needle (2 μm tip), which acted as a holder for the XRD measurements, enabling data collection during rotation (–90° to +45°) around the vertical axis. The energy of the beam was tuned to 42.7 keV, while the beam was focused to 3 × 8 μm$^2$ (H × V, full-width at half maximum). Sample to detector distance (SDD) and tilt of the detector were initially determined from the powder X-ray diffraction image of a $CeO_2$ standard from NIST (674b) using DIOPTAS (Prescher and Prakapenka 2015) and further refined in CrysAlisPro from Rigaku. The single-crystal data are calibrated by an enstatite crystal. Crystal structures were solved using OLEX2 with a SHELX backend (Dolomanov et al. 2009; Sheldrick 2015). Additional data analysis was conducted with JANA2006 (Petříček et al. 2014). The structural models displayed below were drawn using the software VESTA (Momma and Izumi 2011).

## Brillouin scattering

We collected single-crystal Brillouin scattering spectra from grains selected from sample MA-576, our Al-bearing shy-B sample that contained the highest amount of Al (1.35 atoms pfu). Four crystal platelets were double-side polished to 20–25 μm final thickness, and their orientations were determined by single-crystal XRD at the ECB (see above). The orientations of the four platelets were (–0.5, 0, 0.87), (0.83, –0.56, –0.08), (–0.78, –0.38, 0.49), and (–0.81, –0.59, 0.09). Brillouin scattering experiments at ambient conditions were performed at the laser lab of the Extreme Conditions Science Infrastructure (ECSI) of PETRA III, DESY, Hamburg, established by the GFZ Potsdam. The signal was excited by a Nd:$YVO_4$ laser with a wavelength of 532 nm and output power of 100 mW. The Brillouin spectra were recorded by a six-pass Sandercock tandem Fabry-Perot interferometer. The external scattering angle (i.e., the angle between the incident and scattered light directions outside the sample) was 50°, and the mirror spacing was 6 mm during the measurements. The acoustic velocities of the sample were calculated from the measured Brillouin frequency shift, $\Delta\upsilon_B$, as:

$$v = \frac{\Delta\upsilon_B \lambda_0}{2\sin(\theta/2)} \quad (1)$$

where v is the acoustic velocity, $\lambda_0$ is the laser wavelength of 532 nm, and θ is the external scattering angle. The data set of individual acoustic velocities and corresponding wave vector orientations and polarizations were used to determine the nine independent nonzero elastic coefficients of the Al-shy-B sample. The elastic constants were determined by inverting a set of Christoffel's equations:

$$|C_{ijkl} n_j n_l - \rho v^2 \delta_{ik}| = 0 \quad (2)$$

where $C_{ijkl}$ is the elastic constants, $n_j$ and $n_l$ are the direction cosines of the acoustic wave propagation direction. ρ is the density, v is the acoustic velocity derived from Brillouin frequency shift, and $\delta_{ik}$ is the Kronecker δ. Based on the volume derived from X-ray diffraction data and the composition $Mg_{8.04}Si_{2.17}Al_{1.35}O_{18}H_{7.18}$, the density of MA-576 was calculated to be 3.166(4) g/cm$^3$ (the number in parentheses is 1σ standard deviation on the last digit).

# Results

Table 2 shows the EMPA results and chemical composition for the three samples. Sample MA-399 contains 0.35(3) wt% $Al_2O_3$, which corresponds to 0.04 atoms per formula unit in shy-B. This amount has negligible structural effects, and we will consider this sample as Al-free in our discussion. The two samples MA-575, MA-576 contain 4.05(18) and 11.72(21) wt% $Al_2O_3$, respectively (Table 2). The $H_2O$ contents of the three samples were determined by FTIR absorption and are equal to 8(1), 10(1), and 11(1) wt%, respectively. To calculate the chemical formula, we preferred to take the IR-determined water contents rather than the difference of the EMP sum to 100%. The complete chemical formulas for each synthesis are reported in Table 2. Our results show that water content increases with Al content, which is consistent with the result for shy-B with moderate Al content (0.85 < Al < 1.91 pfu) in Kakizawa et al. (2018). There are minor amounts of ringwoodite coexisting with

**Table 2.** Results of EMPA and IR absorption and chemical formula of Al-bearing shy-B

| | Ideal shy-B | Ma-399[a] | Ma-575[a] | Ma-576[a] |
|---|---|---|---|---|
| $SiO_2$ | 29.11 | 28.58(18) | 26.45(19) | 22.35(16) |
| $Al2O_3$ | 0.00 | 0.35(3) | 4.04(18) | 11.81(21) |
| MgO | 65.08 | 61.41(30) | 59.23(21) | 55.48(26) |
| $H_2O$ | 5.81 | 9.64(34)[b] | 10.26(33)[b] | 10.35(32)[b] |
| Total | 100.00 | 100.00[c] | 100.00[c] | 100.00[c] |
| wt% $H_2O$ FTIR | | 8 ±1 | 10 ± 1 | 11±1 |
| Si | 3.00 | 2.93(4) | 2.62(4) | 2.17(4) |
| Al | 0.00 | 0.04(>1) | 0.47(2) | 1.35(4) |
| Mg | 10.00 | 9.40(11) | 8.75(10) | 8.04(11) |
| H | 4.00 | 5.37(10)[d] | 6.60(15)[d] | 7.18(18)[d] |
| Phases | | shy-B, ringwoodite | shy-B, pyrope | shy-B, pyrope |

[a] n (number of analyses) = 28 (MA-399); n = 12 (MA-575); n = 21 (MA576).
[b] $H_2O$ content calculated as difference of the EMPA sum to 100%.
[c] Fixed value.
[d] Formulas calculated based on the water content measured by IR absorption.

shy-B in MA-399 and pyrope coexisting with Al-bearing shy-B in MA-575 and MA-576, which means that pyrope will coexist with Al-bearing shy-B in Al-rich systems.

In our syntheses, we did not observe complex phase assemblages as reported by Kakizawa et al. (2018). In particular, we did not observe a coexistence of two shy-B phases with different Al contents in the same synthesis run. We propose this is due to the rotating multi-anvil press setup used in our experiments. The rotation of our multi-anvil press during the duration of the experiments ensures the homogeneous distribution of the liquid phase in the capsule. Consequently, all the chemical compositions of different grains of our sample are nearly identical within the uncertainty of our measurements. We did not observe other coexisting high-temperature phases such as δ-AlOOH (Kakizawa et al. 2018) as the temperature of our syntheses was 200–400 °C lower than those of Kakizawa et al. (2018).

Figure 1 shows the FTIR spectra in the OH stretching region of the samples prepared as thin films. In the spectrum of the nominally Al-free shy-B sample (MA-399) we can distinguish two main OH bands ($\nu_1$ and $\nu_2$), which we assign to the vibrations of two different hydroxyl groups according to space group symmetry *Pnn*2 that are consistent with Koch-Müller et al. (2005, 2014) and Trots et al. (2013). With increasing Al-content the frequencies of the OH bands do not change. However, the bands visibly broaden, while at least one additional OH band $\nu_3$ is visible at lower wavenumbers. The intensity of $\nu_3$ increases with increasing Al-content (Fig. 1; Online Materials[1] Fig. S1). In the FTIR spectrum of the sample with the highest Al-content (MA-576) only two very broad OH bands can be distinguished (merging $\nu_1 + \nu_2$ and additional $\nu_3$). In all spectra (Online Materials[1] Fig. S1), a fourth very weak OH band can be identified at higher wavenumbers, e.g., at 3554 cm$^{-1}$ (MA-576). The peak positions, the integral absorbances normalized to 1 cm, and the band widths (FWHM) determined for the thin-film spectra are listed in Online Materials[1] Table S1. The calculated water contents are listed in Table 2. All samples contain more OH than the ideal value pointing to two hydrogen positions. As also indicated by the FTIR spectra, there must be additional hydrogens incorporated in the crystal structure. Low-temperature spectra of sample MA-575 and MA-576 were collected in the hope of reducing the FWHM of the OH bands for a better band assignment. But as shown in Online Materials[1] Fig. S2 there is nearly no change in the spectra with decreasing temperature.

To finally verify the presence of $\nu_3$ and $\nu_4$ in all three samples, we collected spectra of individual crystals in the OH stretching region. The spectra are shown in Online Materials[1] Fig. S1. The spectra are oversaturated in the range of 3450 to 3300 cm$^{-1}$, but the presence of the $\nu_3$ band at lower wavenumbers can clearly be seen also in MA-399. In all three spectra, the very weak band $\nu_4$ at higher wavenumber is clearly present.

FTIR spectra in the range of the lattice vibrations are shown in Figure 2, and their frequencies are reported in Online Materials[1] Table S2. Based on the results of Hofmeister (1999), we assign specific vibrations to the peaks; some peaks remain unassigned (Online Materials[1] Table S3). The spectra of the three samples are very similar—they are dominated by vibrations of tetrahedrally and octahedrally coordinated Si. The main difference between the Al-free sample MA-399 and the Al-bearing sample MA-576 is in the region around 600–700 cm$^{-1}$, and we tentatively assigned the two most prominent bands in the spectrum of the sample MA-576 to vibrations of octahedrally coordinated Al.

Raman spectra in the range of the lattice vibrations are shown in Figure 3. Nine Raman peaks for each Shy-B were fitted, and their frequencies are reported in Online Materials[1] Table S2. Based on the results of Hofmeister (1999), we assign specific vibrations to the peaks; some peaks remain unassigned (Online Materials[1] Table S2). The Raman spectra show that the intensity of the peaks becomes weaker with increasing Al-content (Fig. 3). Similar behavior has been reported in Al-rich phase D, which shows broader and weaker Raman peaks than the Al-free one (Pamato et al. 2015; Xu and Inoue 2019). The values of FWHM show that most peaks broaden with increasing Al content (Table 2), potentially indicating the presence of cationic disorder. Most of the peak positions move to larger wavenumbers with increasing Al content. This observation indicates that the incorporation of Al increases the vibrational frequencies and is compatible with the observed decrease of the unit-cell volume (see below). Raman spectra in the OH stretching region also show increas-

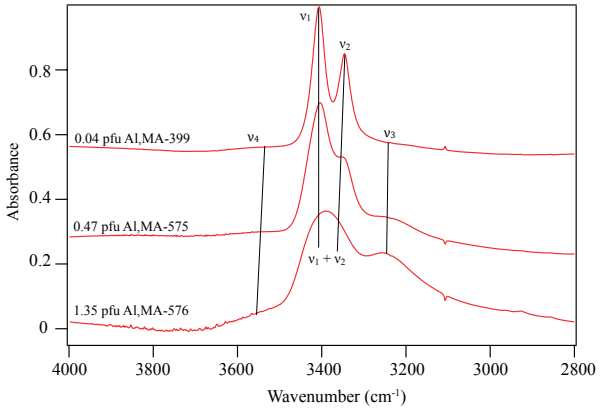


**Figure 1.** Infrared absorption spectra of shy-B samples with different Al contents in the frequency range of the OH stretching vibration.

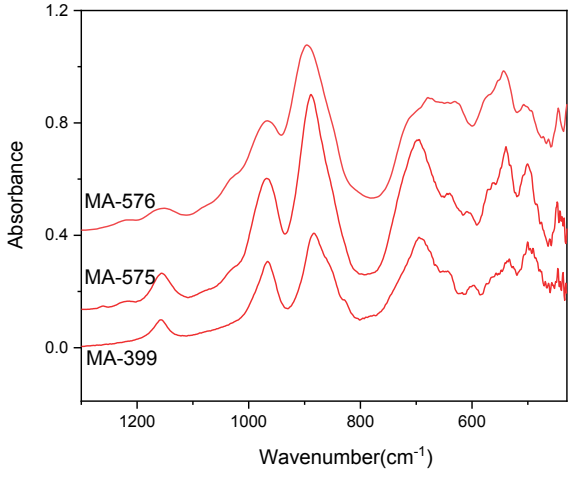


**Figure 2.** Infrared absorption spectra of shy-B samples with different Al contents in the frequency range of the lattice vibrations.

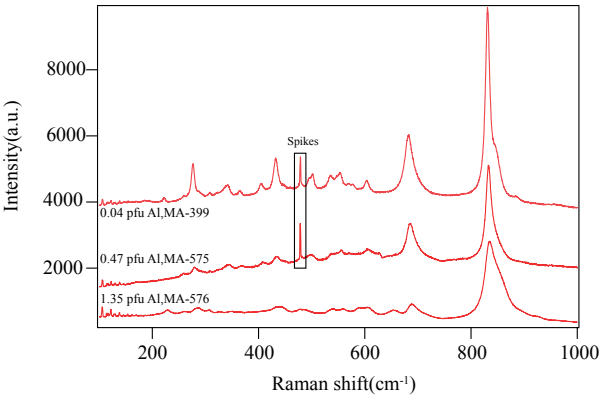


**Figure 3.** Raman spectra of shy-B samples with different Al contents in the frequency range of 100–1000 $cm^{-1}$.

ing peak broadening with increasing Al incorporation (Online Materials[1] Fig. S3).

To examine the structures of shy-B crystals with different Al contents, we performed single-crystal X-ray diffraction refinements at ambient conditions. The details can be found in the CIF files in Online Materials[1]. The unit-cell parameters are also listed in Online Materials[1] Table S3. Although our FTIR results clearly indicate two different hydrogen sites consistent with the space group *Pnn*2 for nominally Al-free shy-B (MA-399), we use both *Pnnm* and *Pnn*2 during the refinement to examine all the possibilities for the other two compositions (MA-575 and MA-576). The main difference between *Pnnm* and *Pnn*2 structural models for shy-B is the description of H atom positions. *Pnnm* has just one general H position (multiplicity 8), while *Pnn*2 has two general H positions (multiplicity 4). Considering the similarity of both space groups and lattice parameters, we can compare them for shy-B with different Al contents (Fig. 4). Our single-crystal refinement shows that the *Pnnm* and *Pnn*2 have the same cell parameters. Figure 4 shows that the incorporation of 1 Al pfu will reduce *a*, *b*, *c* unit-cell parameters and the volume (*V*) of Al-bearing shy-B by 0.69, 0.24, 0.16, and 0.29%, respectively.

Apart from the lattice parameters, the incorporation of Al affects various structural features, including the volumes of $MgO_6$, $SiO_4$, and $SiO_6$ polyhedra. Based on the results of our analysis, we can also compare the volume of the different $MgO_6$ octahedra as a function of Al content (Fig. 5; Online Materials[1] Fig. S4). To simplify the discussion, it seems justified to continue using *Pnnm* as a reference. Indeed, the octahedral sites of Mg5, Mg6, Mg7 in *Pnn*2 are structurally related to those of Mg3, Mg4,

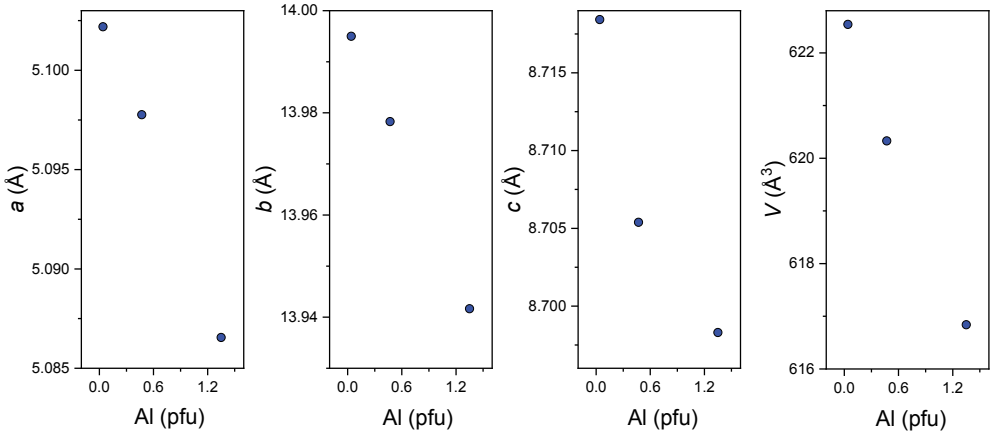


**Figure 4.** Unit-cell parameters and unit-cell volume of shy-B with different Al contents. Error bars are smaller than the symbols.

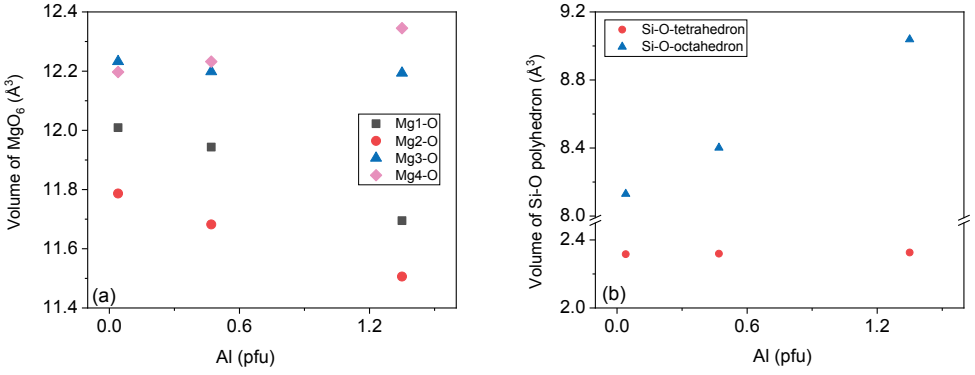


**Figure 5.** Polyhedral volumes of various Mg and Si sites for shy-B with different Al contents in *Pnnm* space group. (**a**) Dependence of the volumes of $MgO_6$ octahedra on the Al content. Squares, circles, triangles, and diamonds represent the octahedral volume for the site of Mg1, Mg2, Mg3, and Mg4, respectively. (**b**) Dependence of the volumes of $SiO_6$ octahedron and $SiO_4$ tetrahedron on the Al content; triangles and circles represent the octahedron and tetrahedron of $SiO_6$ and $SiO_4$, respectively. Error bars are smaller than the symbols in both the panels.

Mg1 in *Pnnm*. In fact, the solutions for both space groups are very close in terms of atomic positions and interatomic distances. This is not surprising, given that the difference between the space groups arises from the symmetry break due to the position of H, the atom with the lowest *Z*, which weakly contributes to X-ray diffraction.

As the Al content in shy-B increases, the volume of the Mg1 and Mg2 octahedra are reduced, in contrast to a slightly increased volume of Mg4 octahedron. The changes of Mg3 octahedron volume are insignificant (Fig. 5). The sites containing Si behave differently as Al content changes, i.e., the volume increases with increasing Al content for $SiO_6$ octahedra but remains unchanged for $SiO_4$ tetrahedra (Fig. 5), indicating a low probability of Al substitution at the latter site.

To put tighter constraints on elasticity, we collected Brillouin scattering spectra and determined acoustic velocities from four crystal platelets, even though two platelets have similar orientations (Fig. 6). Due to the extensive data set, the inversion to determine the full elastic tensor yielded unambiguous results. The fitting results are shown in Figure 6, and the elastic stiffness coefficients are listed in Table 3. Al-bearing shy-B shows lower $C_{11}$, $C_{44}$, $C_{55}$, $C_{13}$, $C_{66}$ but higher $C_{22}$, $C_{12}$ than Al-free end-member and similar $C_{33}$, $C_{23}$. The adiabatic bulk modulus ($K_S$) and the shear modulus ($G$) were estimated to be 140.7(7) and 88.2(4) GPa, respectively, which are also lower than the Al-free

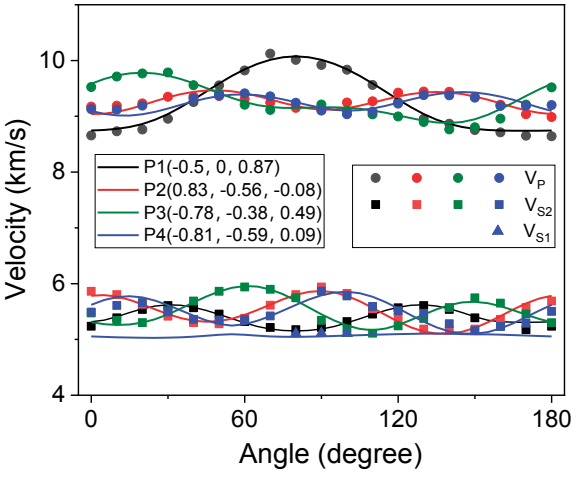


**Figure 6.** Acoustic velocities of shy-B with 1.35 Al pfu (sample MA-576) measured on four platelets with different orientations. Circles: quasi-longitudinal acoustic velocity; squares: fast quasi-shear acoustic velocity; triangles: slow quasi-shear acoustic velocity; curves: fitting results; black, red, green, and blue colors represent the orientations of (–0.5, 0, 0.87), (0.83, –0.56, –0.08) (–0.78, –0.38, 0.49) and (–0.81, –0.59, 0.09), respectively.

composition. The azimuthal $V_P$ anisotropy and maximum $V_S^{PO}$ splitting are calculated using the following equations:

$$A_P = \frac{V_{Pmax} - V_{Pmin}}{V_{Pavg}} \times 100$$

$$A_S^{PO} = \frac{\mathrm{Max}(V_{S2} - V_{S1})}{V_{Savg}} \times 100$$

where $V_{Pmax}$, $V_{Pmin}$, $V_{Pavg}$, are maximum, minimum, and average $V_P$ in the crystal structure. Max ($V_{S2} - V_{S1}$), describes the maximum difference between $V_{S2}$ and $V_{S1}$ in the same propagation direction; $V_{Savg}$ computes the average of all the $V_S$. The values of $A_P$ and $A_S^{PO}$ are 20.1 and 15.9%, respectively.

## Discussion

### Incorporation of H and Al in the structure of shy-B

Based on our single-crystal X-ray refinements of shy-B with different Al contents, we can infer the mechanisms of Al incorporation in the shy-B structure based on the volume of $MgO_6$ and $SiO_6$ octahedra. In the structure of $Al_2O_3$ (corundum structure), MgO (periclase structure), and $SiO_2$ (rutile structure), used as simple references, the volume of $AlO_6$ octahedra is larger than that of the $SiO_6$ octahedra but smaller than the $MgO_6$ octahedra (Online Materials[1] Fig. S5). Based on this simple comparison, we expect to a first-order approximation that the incorporation of Al by substitution of Si in octahedral sites will increase the volume of the octahedra while it will lower the volume of the octahedra when it substitutes Mg. We observe that with increasing Al content in shy-B, the volume of the $SiO_4$ tetrahedral site remains unchanged and that of the $SiO_6$ octahedron becomes larger (Fig. 5) indicating that $Al^{3+}$ substitutes for the octahedral $Si^{4+}$, which is consistent with the Al substitution in stishovite (Bromiley et al. 2006; Litasov et al. 2007a). The volumes of Mg1 and Mg2 octahedral sites decrease with increasing Al content, indicating a preferred Al substitution for Mg in Mg1 and Mg2 (if we refer to the *Pnnm* space group). The volume of the Mg3 octahedron remains unaffected by the change in Al content suggesting that the substitution of Al in Mg3 octahedra site is negligible. In contrast, the volume of the Mg4 octahedral site slightly increases with increasing Al content, indicating a presence of Al in Mg4 octahedral site is limited. The increase of Mg4 octahedron might be caused by vacancies in this site.

The hydrogen positions and OH dipole directions of the stoichiometrically incorporated hydrogens are well known from neutron diffractions data and polarized FTIR spectra on oriented crystals (Trots et al. 2013; Koch-Müller et al. 2014); the two main OH bands in MA-399 are assigned to these two

**Table 3.** Elastic tensor of shy-B with different composition measured at ambient conditions

| Composition | Density (g/cm³) | $C_{11}$ (GPa) | $C_{22}$ (GPa) | $C_{33}$ (GPa) | $C_{44}$ (GPa) | $C_{55}$ (GPa) | $C_{66}$ (GPa) | $C_{12}$ (GPa) | $C_{13}$ (GPa) | $C_{23}$ (GPa) | $K_S$ (GPa) | $G$ (GPa) | Reference |
|---|---|---|---|---|---|---|---|---|---|---|---|---|---|
| $Mg_{8.08}Al_{1.35}Si_{2.17}H_{7.18}O_{18}$ | 3.166(4) | 216.8(28) | 324.4(13) | 285.4(15) | 82.9(10) | 83.3(17) | 85(1) | 73.7(2.0) | 78.0(25) | 76.2(15) | 140.7(7) | 88.2(4) | This study (MA-576) |
| $Mg_{9.38}Si_{2.81}H_{6.01}O_{18}$ | 3.197(3) | 268(2) | 293(3) | 278(2) | 90(1) | 92(2) | 86(1) | 68(5) | 87(2) | 70(2) | 143.1(9) | 94.1(5) | Li et al. (2016) |
| $Mg_{10.4}Si_{3.1}H_{2.7}O_{18}$ | 3.339(4) | 280(2) | 309(2) | 289(2) | 90(1) | 100(1) | 91(1) | 67(1) | 94(2) | 75(2) | 150.2(15) | 98.5(9) | Rosa et al. (2015) |
| $Mg_{9.69}Si_{2.88}H_{5.1}O_{18}$ | 3.239(4) | 271.6(19) | 299.7(19) | 280.3(19) | 87.3(9) | 97(1) | 88.3(1) | 65(1) | 91.2(19) | 72.7(19) | 145.7(15) | 95.5(9) | Revalued[a] |
| $Mg_{10}Si_3H_4O_{18}$ | 3.327 | 280(15) | 307.4(16) | 293.4(14) | 90(11) | 99.2(08) | 89.6(08) | 66.1(22) | 105.6(26) | 81.8(26) | 154.0(42) | 97.0(7) | Pacalo and Weidner (1996) |

[a] Recalculated results of Rosa et al. (2015) by the suggestion from Li et al. (2016).

OH dipoles, and their vibrations are labeled as $\nu_1$ and $\nu_2$. In the thin-film spectra there may be hints for two additional OH bands $\nu_3$ and $\nu_4$. To have a better insight into the defect H, we collected low-temperature spectra and spectra on relatively thick crystals (Online Materials[1] Figs. S1 and S2). There is nearly no change in the OH bands with decreasing temperatures. The bands remain broad, indicating that the large FWHM is caused by cationic disorder rather than by thermal broadening. According to Trots et al. (2013) both non-defect hydrogens are coordinated by Mg1, Mg2, and Mg3 sites. We suggest that Al-substituting Mg in Mg1 and Mg2, as shown in this study, leads to variable environments of the hydrogen and thus to the observed higher band widths. Figure 1 and Online Materials[1] Figure S1 clearly show that defect hydrogen is present in all three samples. The intensity of the band $\nu_3$ at 3261 $cm^{-1}$ (MA-399) increases with increasing vacancies of the Mg sites for samples MA-575 and MA-576, and thus we assigned the band to this defect. The band $\nu_4$ is also present in all three samples, however, only with a constant and minor intensity. We will discuss its possible origin later on.

Due to the very limited Al content in MA-399 whose composition is $(Mg_{9.39}\square_{0.61})(Si_{2.93}Al_{0.04}\square_{0.03})H_{5.37}O_{18}$, we considered it as Al-free shy-B in this discussion. The extra 1.37 H pfu goes to the tetrahedral silicon site as hydrogarnet substitution (0.12 H pfu), vacancies in the Mg site (1.22 H pfu) and neglectable 0.04 H pfu goes to Si octahedral site by the mechanism of $Si^{4+} = Al^{3+} + H^+$.

Based on our single-crystal structural models and electron microprobe analyses of the Al-bearing samples MA-575 and MA-576, we propose the following coupled substitutions for Al-bearing shy-B: (1) $Si^{4+} = Al^{3+} + H^+$; (2) $2\,Al^{3+} = Mg^{2+} + Si^{4+}$; (3) $Mg^{2+} = \square^{Mg^{2+}} + 2H^+$ ($\square^{Mg^{2+}}$ means vacancy in Mg site). As the ionic size of $^{VI}Al^{3+}$ and $^{VI}Si^{4+}$ are quite similar (Shannon 1976), we propose that $Al^{3+}$ first occupies all the Si octahedral sites and then the other sites. We rule out the possibility of large contributions from the hydrogarnet substitution as the X-ray refinement indicates fully occupied (Si+Al) tetrahedral and octahedral Si sites. However, a limited amount as observed in MA-399 may be possible.

Sample MA-575 contains 0.47 Al pfu in total ($Mg_{8.75}Al_{0.47}Si_{2.62}H_{6.60}O_{18}$). 0.38 Al pfu is needed to occupy all the Si octahedral sites, and the remaining 0.09 Al pfu goes to the Mg site. We thus assign 0.29 Al to the octahedral Si-site via mechanism 1; 0.09 Al pfu (in total) goes to Mg1 and Mg2 sites and 0.09 pfu $Al^{3+}$ to the octahedral Si site by mechanism 2. Therefore, the residual charge in the Si site should be balanced via mechanism 1 by 0.29 H pfu. Vacancies in the Mg sites are charge balanced by mechanism 3, resulting in 2.32 H pfu. The crystal-chemical formula for MA-575 can thus be stated as $(Mg_{8.75}Al_{0.09}\square_{1.16})(Si_{2.62}Al_{0.38})H_{6.60}O_{18}$.

Following the substitution mechanisms as described for MA-575, the crystal-chemical formula of MA-576 will be $(Mg_{8.04}Al_{0.52}\square_{1.44})(Si_{2.17}Al_{0.83})H_{7.18}O_{18}$: 0.31 Al pfu assigned to the octahedral Si site via mechanism 1 results in 0.31 $H^+$ pfu; 0.52 Al pfu (in total) is in the Mg1 and Mg2 sites and 0.52 Al pfu in the octahedral Si site via mechanism 2; vacancies in the Mg sites are charge balanced by mechanism 3 resulting in 2.88 additional H pfu.

In summary, with increasing Al-incorporation in shy-B the Mg vacancy content and Al incorporation into the octahedral Si site increase, and both lead to an increasing H content.

The assignment is consistent with the FTIR spectra: the increasing absorbance of the band $\nu_3$ with increasing Al-content is due to increasing Mg vacancies content (0.6, 1.16, and 1.44 pfu, in MA-399, MA-575, and MA-576, respectively), and charge balance via mechanism 2 resulting in 1.4, 2.32, and 2.88 $H^+$ pfu. In the nominally Al-free sample MA-399 the absorption band $\nu_3$ is weak but still clearly visible (Online Materials[1] Fig. S1; see also Online Materials[1] Table S1). There should be additional weak OH bands due to mechanism 1 in the FTIR spectra of MA-575 (0.29 H) and MA-576 (0.31 H) but nearly none (0.04 H pfu) in the spectra of MA-399. These additional OH bands should have frequencies close to 3100 $cm^{-1}$ based on available data for H-bearing Al-stishovite (Bromiley et al. 2006; Litasov et al. 2007a), and they may be hidden in the background. However, we do observe a weak OH band, $\nu_4$, in all three samples, and we tentatively assign it to the hydrogarnet substitution. At least for sample MA-399 the chemical composition analyses indicate 0.03 pfu vacancies in the Si site, which would result in 0.12 H pfu. Due to the complex Al incorporation into the structure and variable vacancies, we cannot rule out that the same holds for MA-575 and MA-576. The hydrogarnet substitution would result in four $OH^-$ bands with a strong band in the frequency range of $\nu_4$; the others may be hidden by the high intrinsic OH bands described above.

Our interpretation of the data is partly consistent with the results of Kakizawa et al. (2021). They investigated one Al-shy-B sample with nearly the same composition as MA-576. The FTIR spectra are quite similar to the spectra of MA-576 shown in Figure 1 and Online Materials[1] Figure S1. In agreement with our conclusions the broad band at 3400 $cm^{-1}$ (our merged $\nu_1$, $\nu_2$) is assigned to the stoichiometrically incorporated hydrogen for *Pnn*2. The band at 3260 $cm^{-1}$ (our band $\nu_3$) and at 3540 $cm^{-1}$ (our band $\nu_4$) are according to Kakizawa et al. (2021) assigned to the substitution mechanism 1 ($Si^{4+} = Al^{3+} + H^+$) and to a new and complex substitution mechanism 4: $2Mg^{2+} = Al^{3+} + H^+ + \square^{Mg^{2+}}$, respectively. This assignment is not supported by our data. We studied three samples with different Al-contents, the band in question ($\nu_3$) is present in all three spectra (Online Materials[1] Fig. S1), but only two of the samples show the substitution of $Si^{4+}$ by $Al^{3+}$ (Table 2). In addition, in our study, the band at 3450 $cm^{-1}$ ($\nu_4$) shows a constant and weak absorption in the spectra of all three samples (Online Materials[1] Fig. S1), which is not consistent with the substitution mechanism in which Mg vacancies are involved as the amount of vacancies increases with Al content.

Al incorporation into the Mg-site (mechanism 2) causes a broadening of the OH absorption bands, which leads to the merging of OH bands $\nu_1$ and $\nu_2$. As observed in other solid solutions systems such as Al-bearing phase D, the partial substitution of Mg by Al at the Mg site results in variable Mg-Al environments for the H sites, and causes band broadening (Xu et al. 2019). We can rule out that the band broadening is due to dynamic disordering of H atom around the normal H position as we see no sharpening of the bands with decreasing temperature (Online Materials[1] Fig. S2). In conclusion, Al-free shy-B with two distinct H atomic positions crystallizes in *Pnn*2 space group and the incorporation of Al into the hydrogen coordinating Mg sites M1 and M2 leads to cationic disorder and seems to result in overlapping unresolved OH bands leaving the question of the ultimate structure type

(*Pnn*2 or *Pnnm*) for Al-rich shy-B unsolved. To gain further structural information, Al-rich shy-B needs to be examined by NMR or neutron diffraction in the future.

### Elasticity of Al-bearing shy-B

The elasticity of Al-free shy-B with different hydrogen contents has been investigated at ambient or high-*P*-*T* conditions using Brillouin scattering (Pacalo and Weidner 1996; Rosa et al. 2015; Li et al. 2016). We list the sets of nine independent elastic constants (at ambient conditions) for the different chemical compositions in Table 3 and we plot them in Figure 7, where the valency of the cations is considered [i.e., for MA-576 (Al+H)/(H+Al+Mg+Si) equates to (3·1.35 + 7.18)/36]. We also recalculated the results of Rosa et al. (2015) using the correct composition (and density) of that sample following the suggestion by Li et al. (2016). The elastic stiffness coefficients of Al-free shy-B show a general decrease with increasing H content, and only $C_{44}$ and $C_{12}$ are insensitive to the H content within uncertainty; the effect of Al incorporation modifies these trends, especially in the case of $C_{11}$, $C_{22}$, and $C_{23}$ (Fig. 7). The incorporation of H in shy-B will significantly reduce the mass per formula unit leading to a sensible decrease of density of shy-B. To better determine the effects of H and Al incorporation on the elasticity and acoustic velocity of shy-B, we try to exclude the effect of density (mostly due to H incorporation) by normalizing the individual coefficients and expressing them as the ratio $C_{ij}$/density. Using the value of $C_{ij}$/density from Pacalo and Weidner (1996) as a reference ideal Mg- end-member of shy-B, we calculated the differences of the individual $C_{ij}$ for each composition of shy-B (Fig. 8). When the effect of density (i.e., of hydrogen incorporation) is removed, the value of most $C_{ij}$/density for Al-free shy-B with different water contents remains equal within uncertainties (Fig. 8). The differences of $C_{12}$, $C_{13}$, and $C_{23}$ are larger, as the off-diagonal elastic coefficients are more difficult to constrain (they cannot be determined independently by individual Brillouin scattering or sound velocity measurements). When we consider the Al-free system in previous studies, the values of $C_{ij}$/density for all the other coefficients are effectively insensitive to the H content indicating that the incorporation of H in excess compared to the ideal Mg- end-member composition will not affect the sound velocity of shy-B, because it equally reduces both the elastic coefficients and the density. When we consider Al-bearing shy-B (MA-576), the elastic coefficients $C_{11}$, $C_{44}$, $C_{55}$, $C_{66}$, and $C_{13}$ are lower, $C_{22}$, $C_{12}$, $C_{23}$, are higher and $C_{33}$ and $C_{66}$ are equal to those of Al-free shy-B. The large difference observed for several density-normalized $C_{ij}$ of Al-bearing shy-B indicates that the substitution of Al in the structure has a much larger impact on the sound velocity of this phase.

To understand the relationship between Al incorporation and elasticity, we need to consider the crystal structure of Al-free shy-B. The structure of shy-B is characterized by an alternation of layers containing octahedra (Mg) and tetrahedra (Si) and layers containing octahedra (Mg) and octahedra (Si) stacked along the *b*-crystallographic axis (Fig. 9). All the available experimental studies of the elastic properties of Al-free shy-B (with variable H contents) and also density functional theory (DFT) studies

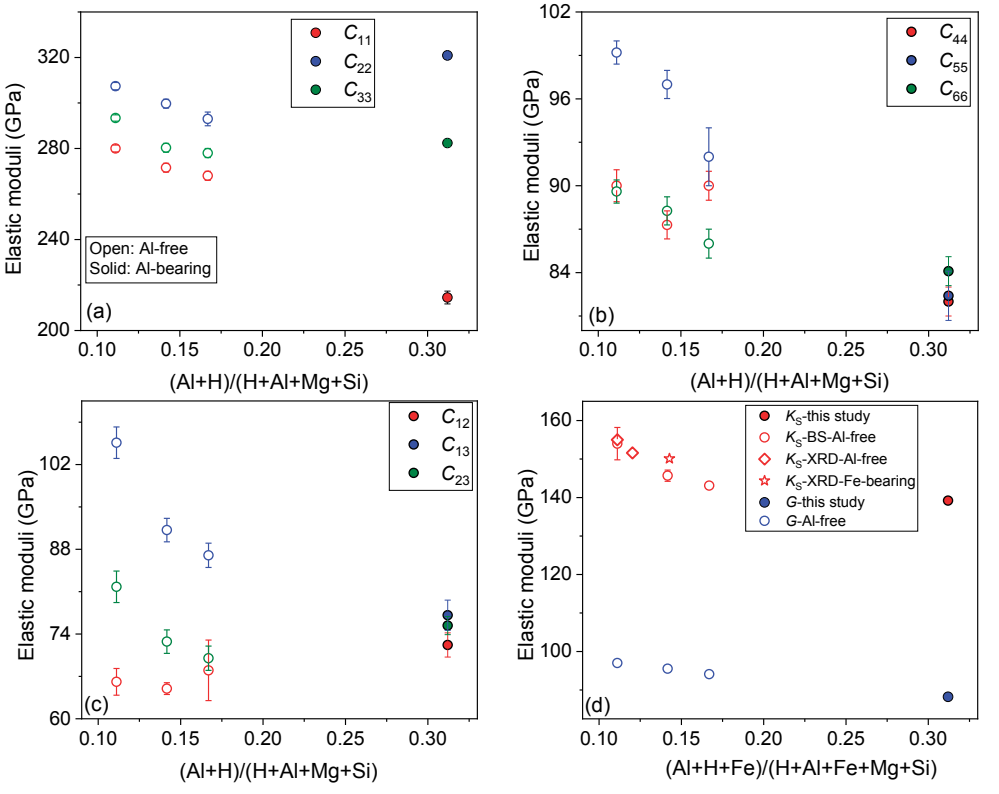


**Figure 7.** Relationship between elastic stiffness coefficients and the amount of H, Al, and Fe incorporated in shy-B. The valency of the cations is considered (i.e., for MA-576 the (Al+H)/(H+Al+Mg+Si) is equal to (3·1.35 + 7.18)/36). The solid circles represent this study for Al-bearing shy-B. The open circles represent the Al-free shy-B with different water contents from previous studies (Pacalo and Weidner. 1996; Rosa et al. 2015; Li et al. 2016); the open red diamonds in panel **d** represent the isothermal bulk modulus ($K_{T0}$) obtained by X-ray diffraction for Al-free shy-B with different water contents (Litasov et al. 2007b; Inoue et al. 2013); the open red star represents the $K_{T0}$ of Fe-bearing shy-B (Crichton et al. 1999). Error bars smaller than the symbols are not shown in the figures.

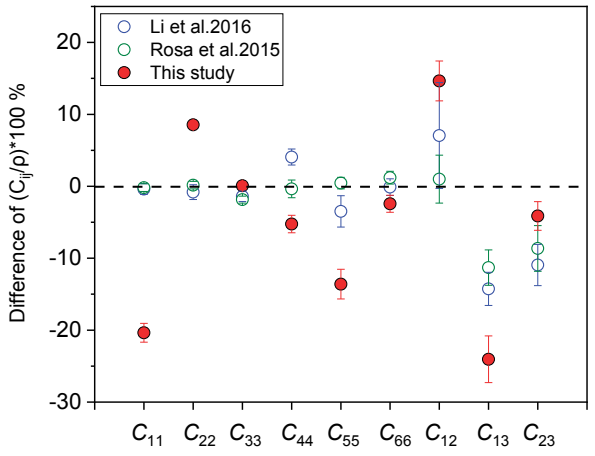


**Figure 8.** Effect of H and Al incorporation on the individual elastic stiffness coefficients of shy-B. The change is expressed as $100 \cdot [(C_{ij}/\text{density})_a - (C_{ij}/\text{density})_{ref}]$, where the subscript a indicates Al-bearing or H-enriched shy-B and the subscript ref indicates ideal Mg-end-member shy-B (Pacalo and Weidner 1996). Solid circles MA-576; open blue circles from Li et al. (2016); open green circles from Rosa et al. (2016).

consistently show that *b* is the stiffest axial direction with $C_{22}$ ~10% larger than $C_{11}$ and ~7% larger than $C_{33}$ (Pacalo and Weidner 1996; Mookherjee and Tsuchiya 2015; Rosa et al. 2015; Li et al. 2016; Yang et al. 2017). The stiffness along the *b*-direction is enhanced by the presence of two different alignments or columns of polyhedral units running along this direction, and it is controlled by the stiffest unit in these alignments. Based on the available data, the stiffness of Si-O tetrahedra is much higher than that of Mg-O and Si-O octahedra (Ottonello 1997). In both columns aligned along *b*, one of the stiff Si-O tetrahedral bonds is systematically aligned parallel to the *b*-axis (Fig. 9). In each column, both Si-tetrahedra and softer Si-octahedra are present with a ratio of 1:1. However, due to a shift along *b*-axis between the two columns, the resulting sequence of layers stacked along *b* have a ratio of tetrahedra-bearing vs. fully octahedral layers of 2:1. The distance between Si atoms aligned along the *b*-columns is a sequence of ~3.5 and ~5.2 Å.

Looking for structural features parallel to the *a*- and *c*-axes, we find that two types of column-like units have either only Si-octahedra or Si-tetrahedra alternating with Mg-octahedra. The distance between Si atoms along the columns running parallel to *a* is equal to the unit-cell parameter *a* (~5 Å). No stiff bond is aligned along the *a*-direction, and the arrangement of the stiff tetrahedra gives the option for rigid rotations to accommodate compression. Column-like structures along the *c*-axis offer a more direct alignment of cations, involving either only Si-octahedra or Si-tetrahedra, at distances equal to the *c* unit-cell parameter (~8.5 Å). However, the packing of polyhedra is denser than along the *a*-axis, with average distances between Si and Mg or Mg and Mg averaging at ~2.7 Å.

The mechanisms through which Al incorporation affects the elastic tensor of shy-B is complicated by the coexisting effects of vacancies and hydrogen incorporation. Below, we interpret the effects on the compressional coefficients $C_{11}$, $C_{22}$, and $C_{33}$ based on our complete set of structural and spectroscopic observations.

We have identified the following major mechanisms: (1) Al incorporation causes a decrease of the unit-cell parameters *a*, *b*, *c*, and potentially stiffening all the $C_{ii}$ (i = 1,2,3); (2) Al substitution at the octahedral Si site softens Si-O octahedra; (3) Al substitution at Mg sites stiffens Mg-O octahedra; (4) vacancies on Mg octahedra make them softer. In the case of $C_{11}$ (the uniaxial stiffness along the *a*-direction) mechanisms 1, 2, and 3 are all active. However, as the distance between Si polyhedra is very large (~5 Å), the shrinking of *a*-axis has a limited effect on $C_{11}$. In addition, in MA-576 a large amount of Si is substituted by Al, and mechanism 2 is dominant over 1 and 3. Consequently, $C_{11}$

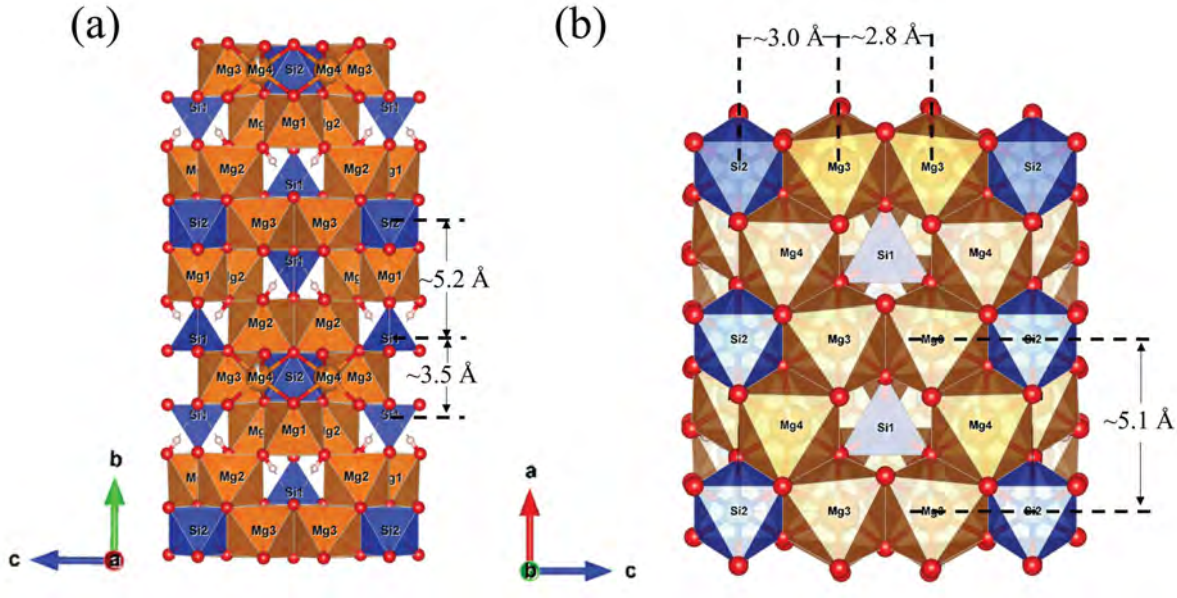


**Figure 9.** Crystal structure of Al-bearing shy-B(MA-576): *b*-*c* plane (**a**) and *a*-*c* plane (**b**).

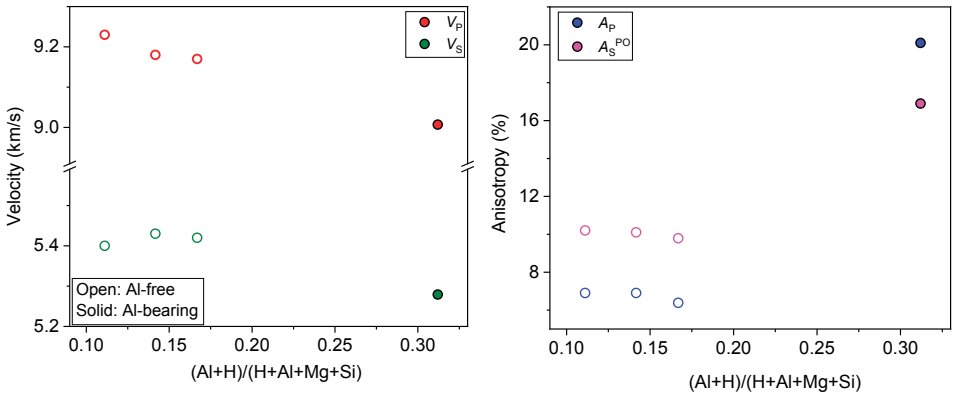


**Figure 10.** Average aggregate sound velocity and acoustic anisotropy of Al-bearing and Al-free shy-B at ambient condition. Solid circles = this study; open circles = Pacalo and Weidner (1996), Rosa et al. (2015), Li et al. (2016). (**left**) Sound velocity of Al-bearing and Al-free shy-B. (**right**) $V_P$ anisotropy and $V_S^{PO}$ splitting of Al-bearing and Al-free shy-B.

softens with respect to Al-free shy-B. In the case of $C_{22}$, as the stiffest Si-O tetrahedral is aligned with the *b*-axis, mechanism 1 will dominate and make $C_{22}$ stiffer. In the case of $C_{33}$ the four different mechanisms balance each other, and the constant is only marginally affected by Al incorporation.

## Implications

Shy-B is potentially a major hydrous phase in cold slabs subducted to the depth of the transition zone and the topmost part of the lower mantle (Schmidt and Ulmer 2004; Ohtani 2005). The presence and decomposition of Al-free shy-B might be related to the low-velocity zone or 720–800 km discontinuity in the shallow lower mantle (Li et al. 2016; Yang et al. 2017). The study by Kakizawa et al. (2018) showed that Al-bearing shy-B has a much wider stability field compared to the Al-free counterpart. Pyrope-rich garnet can be the main Al carrier in the subducted slabs in the deep transition zone and the top of the lower mantle. Our syntheses results show that Al-free shy-B coexists with ringwoodite, while Al-bearing shy-B coexists with pyrope at the conditions of our synthesis runs (Table 2). In the peridotite layer of subducted slabs, Al-free shy-B could be favored compared to Al-bearing shy-B because the amount of available Al is low. On the other hand, in the basaltic layer, where pyrope is the most abundant phase, Al-bearing shy-B would be present coexisting with pyrope-rich garnet if the subducted slab is $H_2O$ rich. The Al-free shy-B decomposes around 30 GPa and 900 K, indicating that it cannot represent a water carrier even at the conditions of a very cold subduction slab (Ohtani et al. 2003). Having wider stability, Al-bearing shy-B with 31.9 wt% $Al_2O_3$ could be stable at 25 GPa and 2300 K and could be a potential water carrier in the topmost lower mantle (Kakizawa et al. 2018). The elastic properties of Al-bearing shy-B are important for our understanding of the low-seismic velocity anomalies and anisotropy anomalies observed in the transition zone and the topmost part of the lower mantle. Our study demonstrates that while the incorporation of additional $H_2O$ in shy-B mainly affects the density and has only a slight effect on sound velocity (Fig. 8; Table 3), the incorporation of Al has a more complex effect on density and elasticity, resulting in a relevant effect on sound velocity and anisotropy. Comparing aggregate $V_P$ and $V_S$ with those of standard Al-free shy-B, Al-bearing shy-B has 1.8% and 2.6% lower $V_P$ and $V_S$, respectively (Fig. 10). A previous study of sound velocity of $H_2O$-rich Al-free shy-B at high *P*-*T* has shown that the presence of shy-B could help explain the low-velocity zone at the topmost lower mantle but cannot help understand high-anisotropy regions (Li et al. 2016). Our Al-bearing shy-B displays densities that are comparable to those of the $H_2O$-rich Al-free shy-B investigated by Li et al. (2016), which has similar $H_2O$ content (Table 3). At ambient conditions, Al-bearing shy-B has the lowest acoustic velocities among all the previously investigated shy-B compositions (Fig. 10). More importantly, the $V_P$ anisotropy and $V_S^{PO}$ splitting of Al-bearing shy-B are 13.2 and 6.1% higher than those of Al-free one (Fig. 10). The volume fraction of shy-B in the hydrated pyrolite system can reach 25% at pressures of the topmost lower mantle (Ohtani et al. 2005). Assuming a similar pressure and temperature dependence of the elastic tensor as Al-free shy-B (Li et al. 2016), the presence of 25 vol% of Al-bearing shy-B in deep subducted slabs may produce observable lower seismic velocity at topmost lower mantle. More interestingly, as Al-bearing has higher elastic anisotropy than Al-free shy-B, we thus conclude that 25 vol% of Al-bearing shy-B with strong lattice preferred orientation (LPO) might cause ~2% anisotropy for $V_S$ and help understand the anomalous seismic features observed inside and in the proximity of Tonga deep subducted slab (Chen and Brudzinski 2003). However, our study only focuses on the elasticity at ambient conditions, and a high-*P*-*T* study on the elasticity of Al-bearing shy-B is needed in future.

## Acknowledgments and Funding

We acknowledge the scientific exchange and support of the Center for Molecular Water Science (CMWS) as part of the early science program (DESY) and GFZ. Andreas Ebert and Reiner Schulz for the support during the multi-anvil syntheses. We thank Sergey Lobanov for the thickness measurement of the thin films. We also acknowledge DESY (Hamburg, Germany), a member of the Helmholtz Association HGF, for the provision of experimental facilities. Parts of this research were carried out at beamline P02.2 and the Extreme Condition Science Infrastructure (ECSI) of PETRAIII.

## References cited

Boffa Ballaran, T., Frost, D.J., Miyajima, N., and Heidelbach, F. (2010) The structure of a super-aluminous version of the dense hydrous-magnesium silicate phase D. American Mineralogist, 95, 1113–1116.

Bromiley, G.D., Bromiley, F.A., and Bromiley, D.W. (2006) On the mechanisms for H and Al incorporation in stishovite. Physics and Chemistry of Minerals, 33, 613–621.

Chen, W.-P., and Brudzinski, M.R. (2003) Seismic anisotropy in the mantle transition

zone beneath Fiji-Tonga: Seismic anisotropy in the mantle transition zone. Geophysical Research Letters, 30, 1682.
Crichton, W.A., Ross, N.L., and Gasparik, T. (1999) Equations of state of magnesium silicates anhydrous B and superhydrous B. Physics and Chemistry of Minerals, 26, 570–575.
Deon, F., Koch-Müller, M., Rhede, D., and Wirth, R. (2011) Water and iron effect on the *P-T-x* coordinates of the 410-km discontinuity in the Earth upper mantle. Contributions to Mineralogy and Petrology, 161, 653–666.
Dolomanov, O.V., Bourhis, L.J., Gildea, R.J., Howard, J.A.K., and Puschmann, H. (2009) OLEX2: A complete structure solution, refinement and analysis program. Journal of Applied Crystallography, 42, 339–341.
Frost, D. (1999) The stability of dense hydrous magnesium silicates in Earth's transition zone and lower mantle. In Y. Fei, C. Bertka, and B. Mysen, Eds., Mantle Petrology: Field Observations and High Pressure Experimentation: A Tribute to Francis R. (Joe) Boyd, The Geochemical Society, Special Publication No. 6.
Hallis, L.J., Huss, G.R., Nagashima, K., Taylor, G.J., Halldórsson, S.A., Hilton, D.R., Mottl, M.J., and Meech, K.J. (2015) Evidence for primordial water in Earth's deep mantle. Science, 350, 795–797.
Hazen, R.M., Yang, H., Prewitt, C.T., and Gasparik, T. (1997) Crystal chemistry of superfluorous phase B ($Mg_{10}Si_3O_{14}F_4$): Implications for the role of fluorine in the mantle. American Mineralogist, 82, 647–650.
Hofmeister, A.M. (1999) Mantle values of thermal conductivity and the geotherm from phonon lifetimes. Science, 283, 1699–1706.
Inoue, T., Ueda, T., Higo, Y., Yamada, A., Irifune, T., and Funakoshi, K.-I. (2013) High-pressure and high-temperature stability and equation of state of superhydrous phase B. In S.D. Jacobsen and S. Van Der Lee, Eds., Earth's Deep Water Cycle, Geophysical Monograph Series, p. 147–157. American Geophysical Union.
Kakizawa, S., Inoue, T., Nakano, H., Kuroda, M., Sakamoto, N., and Yurimoto, H. (2018) Stability of Al-bearing superhydrous phase B at the mantle transition zone and the uppermost lower mantle. American Mineralogist, 103, 1221–1227.
Kakizawa, S., Inoue, T., and Kuribayashi, T. (2021) Single-crystal X-ray structure refinement of Al-bearing superhydrous phase B. Physics and Chemistry of Minerals, 2021, 48, 1–11.
Koch-Müller, M., Dera, P., Fei, Y., Hellwig, H., Liu, Z., Orman, J.V., and Wirth, R. (2005) Polymorphic phase transition in Superhydrous Phase B. Physics and Chemistry of Minerals, 32, 349–361.
——— (2014) Erratum to: Polymorphic phase transition in Superhydrous Phase B. Physics and Chemistry of Minerals, 41, 725.
Li, X., Mao, Z., Sun, N., Liao, Y., Zhai, S., Wang, Y., Ni, H., Wang, J., Tkachev, S.N., and Lin, J.-F. (2016) Elasticity of single-crystal superhydrous phase B at simultaneous high pressure-temperature conditions: Elasticity of shy-B. Geophysical Research Letters, 43, 8458–8465.
Li, X., Liu, Y., Wang, R., Yoshino, T., Xu, J., Zhang, D., Grützner, T., Zhang, J., and Wu, X. (2021) Thermal equation of state of F-bearing superhydrous phase B ($Mg_{10}Si_3O_{14}(OH,F)_4$): Implications for the transportation of fluorine and water into Earth's lower mantle. Physics of the Earth and Planetary Interiors, 106824.
Libowitzky, E., and Rossman, G.R. (1997) An IR absorption calibration for water in minerals. American Mineralogist, 82, 1111–1115.
Litasov, K., and Ohtani, E. (2003) Stability of various hydrous phases in CMAS pyrolite-$H_2O$ system up to 25 GPa. Physics and Chemistry of Minerals, 30, 147–156.
Litasov, K.D., Kagi, H., Shatskiy, A., Ohtani, E., Lakshtanov, D.L., Bass, J.D., and Ito, E. (2007a) High hydrogen solubility in Al-rich stishovite and water transport in the lower mantle. Earth and Planetary Science Letters, 262, 620–634.
Litasov, K.D., Ohtani, E., Ghosh, S., Nishihara, Y., Suzuki, A., and Funakoshi, K. (2007b) Thermal equation of state of superhydrous phase B to 27GPa and 1373K. Physics of the Earth and Planetary Interiors, 164, 142–160.
Liu, Z., Irifune, T., Nishi, M., Tange, Y., Arimoto, T., and Shinmei, T. (2016) Phase relations in the system $MgSiO_3$–$Al_2O_3$ up to 52 GPa and 2000 K. Physics of the Earth and Planetary Interiors, 257, 18–27.
Liu, Z., Nishi, M., Ishii, T., Fei, H., Miyajima, N., Boffa Ballaran, T., Ohfuji, H., Sakai, T., Wang, L., and Shcheka, S. and others (2017) Phase relations in the system $MgSiO_3$-$Al_2O_3$ up to 2300 K at lower mantle pressures: Phase relations and Al in Bridgmanite. Journal of Geophysical Research: Solid Earth, 122, 7775–7788.
Lobanov, S.S., Schifferle, L., and Schulz, R. (2020) Gated detection of supercontinuum pulses enables optical probing of solid and molten silicates at extreme pressure–temperature conditions. Review of Scientific Instruments, 91, 053103.
Mao, Z., and Li, X. (2016) Effect of hydration on the elasticity of mantle minerals and its geophysical implications. Science China Earth Sciences, 59, 873–888.
Matrosova, E.A., Welch, M.D., Bobrov, A.V., Bindi, L., Pushcharovsky, D.Y., and Irifune, T. (2019) Incorporation of Ti into the crystal structures of the high-pressure dense silicates anhydrous phase B and superhydrous phase B. Physics and Chemistry of Minerals, 46, 909–920.
Momma, K., and Izumi, F. (2011) *VESTA 3* for three-dimensional visualization of crystal, volumetric and morphology data. Journal of Applied Crystallography, 44, 1272–1276.
Mookherjee, M., and Tsuchiya, J. (2015) Elasticity of superhydrous phase, B, $Mg_{10}Si_3O_{14}(OH)_4$. Physics of the Earth and Planetary Interiors, 238, 42–50.
Mrosko, M., Koch-Müller, M., McCammon, C., Rhede, D., Smyth, J.R., and Wirth, R. (2015) Water, iron, redox environment: effects on the wadsleyite-ringwoodite phase transition. Contributions to Mineralogy and Petrology, 170, 9.
Nishi, M., Irifune, T., Tsuchiya, J., Tange, Y., Nishihara, Y., Fujino, K., and Higo, Y. (2014) Stability of hydrous silicate at high pressures and water transport to the deep lower mantle. Nature Geoscience, 7, 224–227.
Ohtani, E. (2005) Water in the mantle. Elements, 1, 25–30.
Ohtani, E., Toma, M., Kubo, T., Kondo, T., and Kikegawa, T. (2003) In situ X-ray observation of decomposition of superhydrous phase B at high pressure and temperature. Geophysical Research Letters, 30, 1029.
Ottonello, G. (1997) Principles of Geochemistry. Columbia University Press, p. 61–62.
Pacalo, R.E.G., and Parise, J.B. (1992) Crystal structure of superhydrous B, a hydrous magnesium silicate synthesized at 1400 °C and 20 GPa. American Mineralogist, 77, 681–684.
Pacalo, R.G., and Weidner, D. (1996) Elasticity of superhydrous B. Physics and Chemistry of Minerals, 23, 520–525.
Palot, M., Jacobsen, S.D., Townsend, J.P., Nestola, F., Marquardt, K., Miyajima, N., Harris, J.W., Stachel, T., McCammon, C.A., and Pearson, D.G. (2016) Evidence for $H_2O$-bearing fluids in the lower mantle from diamond inclusion. Lithos, 265, 237–243.
Pamato, M.G., Myhill, R., Boffa Ballaran, T., Frost, D.J., Heidelbach, F., and Miyajima, N. (2015) Lower-mantle water reservoir implied by the extreme stability of a hydrous aluminosilicate. Nature Geoscience, 8, 75–79.
Pearson, D.G., Brenker, F.E., Nestola, F., McNeill, J., Nasdala, L., Hutchison, M.T., Matveev, S., Mather, K., Silversmit, G., Schmitz, S., Vekemans, B., and Vincze, L. (2014) Hydrous mantle transition zone indicated by ringwoodite included within diamond. Nature, 507, 221–224.
Peslier, A.H. (2020) The origins of water. Science, 369, 1058–1058.
Petříček, V., Dušek, M., and Palatinus, L. (2014) Crystallographic Computing System JANA2006: General features. Zeitschrift für Kristallographie—Crystalline Materials, 229, 345–352.
Prescher, C., and Prakapenka, V.B. (2015) DIOPTAS: a program for reduction of two-dimensional X-ray diffraction data and data exploration. High Pressure Research, 35, 223–230.
Rosa, A.D., Sanchez-Valle, C., Wang, J., and Saikia, A. (2015) Elasticity of superhydrous phase B, seismic anomalies in cold slabs and implications for deep water transport. Physics of the Earth and Planetary Interiors, 243, 30–43.
Schmidt, M.W., and Ulmer, P. (2004) A rocking multianvil: elimination of chemical segregation in fluid-saturated high-pressure experiments. Geochimica et Cosmochimica Acta, 68, 1889–1899.
Sheldrick, G.M. (2015) Crystal structure refinement with *SHELXL*. Acta Crystallographica, C71, 3–8.
Shieh, S.R., Mao, H., Hemley, R.J., and Ming, L.C. (2000) In situ X-ray diffraction studies of dense hydrous magnesium silicates at mantle conditions. Earth and Planetary Science Letters, 177, 69–80.
Trots, D.M., Kurnosov, A., Manthilake, M.A.G.M., Ovsyannikov, S.V., Akselrud, L.G., Hansen, T., Smyth, J.R., and Frost, D.J. (2013) The determination of hydrogen positions in superhydrous phase B. American Mineralogist, 98, 1688–1692.
Tschauner, O., Huang, S., Greenberg, E., Prakapenka, V.B., Ma, C., Rossman, G.R., Shen, A.H., Zhang, D., Newville, M., Lanzirotti, A., and Tait, K. (2018) Ice-VII inclusions in diamonds: Evidence for aqueous fluid in Earth's deep mantle. Science, 359, 1136–1139.
Walker, D., Carpenter, M.A., and Hitch, C.M. (1990) Some simplifications to multianvil devices for high pressure experiments. American Mineralogist, 75, 1020–1028.
Xu, C., and Inoue, T. (2019) Melting of Al-Rich phase D up to the uppermost lower mantle and transportation of $H_2O$ to the deep Earth. Geochemistry, Geophysics, Geosystems, 20, 4382–4389.
Xue, X., Kanzaki, M., and Shatskiy, A. (2008) Dense hydrous magnesium silicates, phase D, and superhydrous B: New structural constraints from one- and two-dimensional $^{29}Si$ and $^{1}H$ NMR. American Mineralogist, 93, 1099–1111.
Yang, D., Wang, W., and Wu, Z. (2017) Elasticity of superhydrous phase B at the mantle temperatures and pressures: Implications for 800 km discontinuity and water flow into the lower mantle: High *PT* elasticity of superhydrous phase. Journal of Geophysical Research: Solid Earth, 122, 5026–5037.

Manuscript received January 26, 2021
Manuscript accepted September 1, 2021
Manuscript handled by Zhicheng Jing

## Endnote:

[1]Deposit item AM-22-57879, Online Materials. Deposit items are free to all readers and found on the MSA website, via the specific issue's Table of Contents (go to http://www.minsocam.org/MSA/AmMin/TOC/2022/May2022_data/May2022_data.html). The CIF has been peer reviewed by our Technical Editors.